



Article

Magnetic Field Analysis and Development of Disk Axial–Radial Hybrid Excitation Generator for Range Extenders in Extended-Range Electric Vehicles

Jianwei Ma ^{1,2}

¹ Department of Automotive Engineering, Hebei Vocational University of Technology and Engineering, Xingtai 054000, China; majianwei01@xpc.edu.cn; Tel.: +86-189-3192-3929

² Hebei Special Vehicle Modification Technology Innovation Center, Xingtai 054000, China

Abstract: Extended-range electric vehicles have both a motor and an engine; the motor is used for driving, and the engine generates electricity via a range extender, which is connected to the motor. The permanent magnet generator is part of the range extender, and the output voltage is controlled by adjusting the engine's speed; the generator's rotating speed fluctuates, meaning that the engine's fuel consumption increases. Meanwhile, considering the limited axial dimension of the range extender, an axial–radial disk hybrid generator that combines excitation is developed, making full use of the radial space; at the same time, the output voltage is adjusted without changing the engine's speed. In this study, the generator's magnetic field hybrid principle, the path of permanent magnetic circuit, and the electric excitation magnetic circuit under different loads were analyzed and verified via the finite element method. A comparative analysis method was also used, the technical index of the disk hybrid excitation generator was determined, and the main structural parameters were designed using theoretical calculations. The three-dimensional finite element model was established based on the results, and a finite element analysis was performed. An equivalent magnetic circuit model was established, and the formulas of synthetic permeability, leakage permeability, and effective permeability were determined. The finite element method (numerical method) and equivalent magnetic circuit method (analytical method) were used to calculate the synthetic magnetic fields of the air gap, rotor yoke, and rotor teeth under different excitation currents. A comparison between the two methods verified the design utility. The conclusions provide a valuable point of reference for the development of the disk hybrid excitation generator for use in range extenders in extended-range electric vehicles.

Keywords: extended-range electric vehicles; range extender; disk hybrid excitation; generator; finite element model; equivalent magnetic circuit



Citation: Ma, J. Magnetic Field Analysis and Development of Disk Axial–Radial Hybrid Excitation Generator for Range Extenders in Extended-Range Electric Vehicles. *World Electr. Veh. J.* **2024**, *15*, 94. <https://doi.org/10.3390/wevj15030094>

Academic Editor: Joeri Van Mierlo

Received: 20 December 2023

Revised: 14 February 2024

Accepted: 2 March 2024

Published: 4 March 2024



Copyright: © 2024 by the author. Licensee MDPI, Basel, Switzerland. This article is an open access article distributed under the terms and conditions of the Creative Commons Attribution (CC BY) license (<https://creativecommons.org/licenses/by/4.0/>).

1. Introduction

Due to recent developments in science and technology, people's living standards have improved, the number of vehicles has risen year by year, and exhaust emissions have become more severe. The world is ever more focused on environmental protection, and electric vehicles have been widely recognized as a new solution to reduce vehicle exhaust emissions and avert a fossil fuel energy crisis [1,2]. Compared with pure electric vehicles, extended-range electric vehicles (EREVs) have a longer driving range, and compared with hybrid electric vehicles, EREVs are more environmentally friendly. EREVs adopt the structure of hybrid electric vehicles, and they are especially suitable for use in urban road conditions with frequent starts and stops. They may also help nations to meet their energy conservation and emission reduction targets [3–5].

Therefore, EREVs can solve many problems affecting the vehicle industry, such as driving range, power, emissions, etc., as they combine the advantages of pure electric

vehicles and hybrid electric vehicles. We predict that EREVs represent the future of electric vehicles [6].

The generator is an important part of an EREV's range extender, and it greatly impacts the vehicle's performance. A permanent magnet generator is often used in range extenders both at home and abroad, and the power density of the axial flux permanent magnet motor is higher than that of the radial flux permanent magnet motor. The rotor is typically replaced with a permanent magnet to reduce the motor volume and improve the power density [7].

Ref. [8] considered the main parameters that affect the fundamental amplitude of a no-load voltage and the total harmonic distortion degree of an axial flux permanent magnet motor. The polar arc coefficient of a permanent magnet and side width of a coil were improved using an algorithm. The maximum fundamental amplitude and the minimum harmonic content were the optimization objectives. The optimization design's reliability was verified via finite element simulation.

Ref. [9] used an external rotor permanent magnet synchronous generator to overcome problems associated with high temperatures generated during the application of the range extender. Moreover, the authors designed a variable section channel with turbulent flow. Through the coupling of the magnetic, temperature, and stress fields, the motor was simulated, analyzed, and optimized. The motor's heat dissipation performance was, thus, enhanced. This design also guaranteed a good temperature equalization performance and provided a new idea for designing the cooling system.

However, the hybrid excitation generator used a permanent magnet material and electro-magnetic winding for joint excitation, combining the advantages of an electro-magnetic generator and a permanent magnet generator. It possesses not only the electro-magnetic generator's good adjustment characteristics but also the permanent magnet generator's high power density, efficiency, and reliability. We believe that hybrid excitation generators represent the future of range extender generators [10,11].

Professor Soichi Ishii of Tohoku University, Japan, Professor Zhu Xiaoyong of Jiangsu University, China, and other researchers proposed the potential structure of low-rare-earth permanent magnet motors with combined excitation [12,13]. The motor's rotor had a double-layer permanent magnet structure; the inside of the rotor was made of ferrite, and the outside of the rotor was made of rare earth permanent magnet material. A hybrid excitation motor was proposed by Professor Zhu Ziqiang of the University of Sheffield, United Kingdom: the permanent magnet was fixed on the inner stator teeth in the hybrid excitation motor, the exciting winding was wound in the inner stator slot, and two kinds of excitation sources co-existed to reduce the quantities of rare earth permanent magnet materials and conveniently adjust the magnetic field [14].

Using structural optimization design to improve the utilization of rare earth permanent magnet materials is another important research direction for low-rare-earth permanent magnet motors. It can be increased to change the number and position of the permanent magnet slots to improve the torque density of the motor, as shown in [15]. The permanent magnet slots were divided into three layers: the outermost layer has a 'linear' shape, where there is no permanent magnet, and the other two layers have a 'U' shape, with permanent magnets placed on both sides. In [16], the D-axis inductance was increased by changing the rotor core shape, setting the magnetic barrier, and performing rounding. In addition, a layered magnetic steel structure was proposed, and the structural parameters were optimized to achieve an optimal combination of electro-magnetic torque and magnetoresistive torque. Thus, the volume of the rare earth permanent magnets was reduced [17].

Quan Xiaowei et al. of the Xi'an University of Technology proposed a dual-rotor hybrid excitation axial flux switching generator. The generator had a middle stator and two external rotors. The stator was composed of a number of double H-shaped iron cores and permanent magnets, and the rotor consisted of a disk rotor formed by superimposing silicon steel sheets. The armature coil was wound on the side teeth between the permanent magnet and the H-shaped core, and the excitation winding material was wound on the

middle teeth. The hybrid excitation generator had high torque density and large torque, but as the structure used a dual-rotor structure to balance the axial magnetic tension, there was a double-layer air gap [18].

Ref. [19] established a simulation model of a permanent magnet generator with an external rotor for electric vehicle range extenders using the finite element method. The cogging torque, potential waveform, and harmonic magnitude were improved by installing a reasonable chute. The parameters of the optimal chute angle, air gap, and width of the slot were optimized to maximize the generator's efficiency.

Ref. [20] considered issues related to the optimization of the tooth zone of a homopolar inductor generator with non-overlapping concentrated coils. Recommendations for the tooth zone's optimal parameters were made by analyzing the magnetic field using the machine's cross-section. Ref. [21] discussed various aspects of design optimization for the traction SHMS, using a one-criterion unconstrained Nelder–Mead method; an original two-dimensional finite element model of a SHM was also used, drastically reducing the computational burden, thus enabling objective optimization.

Thus far, many scholars have conducted research into permanent magnet and hybrid excitation generators, but generators for a range extender are mainly permanent magnet generators, the magnetic field of which is not adjustable; it can only rely on adjusting the speed of the range extender's generator to achieve output-voltage stabilization, increasing the engine's fuel consumption. Firstly, to solve the above problems, a disk hybrid excitation generator with a small-sized axial designed for the range extender was installed in the extended-range electric vehicle. According to the structure scheme, the feasibility analysis of the operating principle of the generator was performed by analyzing the magnetic circuit. Secondly, the performance index of the generator was determined; the main structural parameters, such as the permanent magnet, excitation winding, and armature winding, were calculated according to the performance index; and the geometric model was established according to the calculation results. Finally, the formulas of synthetic permeability, leakage permeability, and effective permeability were derived based on the equivalent magnetic circuit model. The magnetic field of the generator was analyzed using the equivalent magnetic circuit method and the finite element method, and the structural parameters were then optimized. The magnetic induction intensity in the generator's air gap, rotor yoke, and rotor tooth were then calculated. The comparison and analysis of the calculation results of the two methods show that the generator's operating principle was feasible and its structure was reasonable. It provided a scientific design method for the development of a hybrid excitation generator for an EREV range extender.

2. Structure Design of Disk Hybrid Excitation Generator

The structure of the disk hybrid excitation generator for an EREV range extender is shown in Figure 1, including outer disk rotor, outer armature winding, combined stator core, permanent magnet, excitation winding, shell, inner disk rotor, inner armature winding, inner rotor teeth, magnetic yoke, excitation core, magnetic insulation sleeve, shaft, and outer rotor teeth. In the structure, the radial permanent magnet flux and axial electro-magnetic flux are synthesized in the outer disk rotor and inner disk rotor for the hybrid excitation, giving the generator high power density and good voltage regulation. In addition, the double air gap symmetry structure, composed of a middle stator and two rotors, balances the axial magnetic pull of the disk hybrid generator.

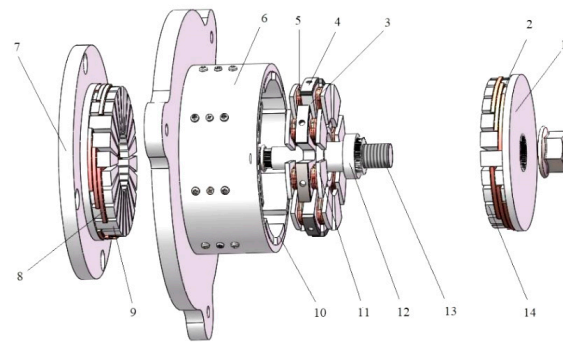


Figure 1. Structure diagram of disk hybrid excitation generator for range extender of EREV. 1. Outer disk rotor, 2. Outer armature winding, 3. Combined stator core, 4. Permanent magnet, 5. Exciting winding, 6. Shell, 7. Inner disk rotor, 8. Inner armature winding, 9. Inner rotor teeth, 10. Magnetic yoke, 11. Excitation core, 12. Magnetic insulation sleeve, 13. Shaft, 14. Outer rotor teeth.

3. Analysis of the Operation Principle of Disk Hybrid Excitation Generator

The disk hybrid excitation generator's shell is connected to the body of the engine, the flywheel is connected to the inner disk rotor to drive the inner disk rotor's rotation, and the inner disk rotor rotates the outer disk rotor with the shaft. During rotation, the radial parts of the outer and inner armature winding cut the synthetic magnetic field, composed of the electro-magnetic and permanent magnetic parts, and induced electromotive force is generated in the outer and the inner armature winding.

According to the change in load, the excitation current is adjusted to adjust the synthesized magnetic field, and the output voltage is stabilized. When the load is low, the magnetic field produced by the permanent magnet meets the requirements. At this point, there is no exciting current in the excitation coil, with only the magnetic flux generated by the permanent magnet present in the magnetic circuit. The magnetic circuit generated by the permanent magnet is shown in Figure 2 and has the following specifications: the N pole of the permanent magnet → magnetic yoke → air gap δ_1 → disk rotor → air gap δ_2 → combined stator core → S pole of the permanent magnet. When the load increases, the generator's output voltage decreases, and a direct exciting current enters the excitation coil to generate the same air gap magnetic flux in the direction of air gap magnetic flux generated by the permanent magnet. The magnetic flux has two parts. (1) The magnetic circuit generated by the permanent magnet is shown in Figure 2 and has the following specifications: N pole of the magnet → magnetic yoke → air gap δ_1 → disk rotor → rotor teeth → air gap δ_2 → excitation core → combined stator core → S pole of the permanent magnet. (2) The magnetic circuit generated by the excitation coil is shown in Figure 3 and has the following specifications: N pole of the excitation core → combined stator core → adjacent excitation core on the same side → air gap δ_1 → rotor teeth → disk rotor → air gap δ_1 → S pole of the excitation core. The directions of the electric field and the permanent magnetic field passing through the armature winding are identical, and the synthetic flux is superimposed on each of them, resulting in the flux being enhanced in the air gap. When the engine rotates the disk rotor, the magnetic flux through the armature winding changes constantly, thus alternating the generated current.

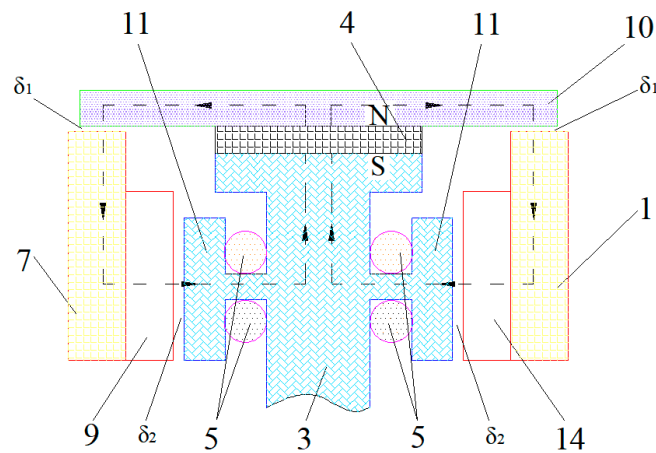


Figure 2. Magnetic circuit diagram of permanent magnet field. 1. Outer disk rotor, 3. Combined stator core, 4. Permanent magnet, 5. Exciting winding, 7. Inner disk rotor, 9. Inner rotor teeth, 10. Magnetic yoke, 11. Excitation core, 14. Outside rotor tooth.

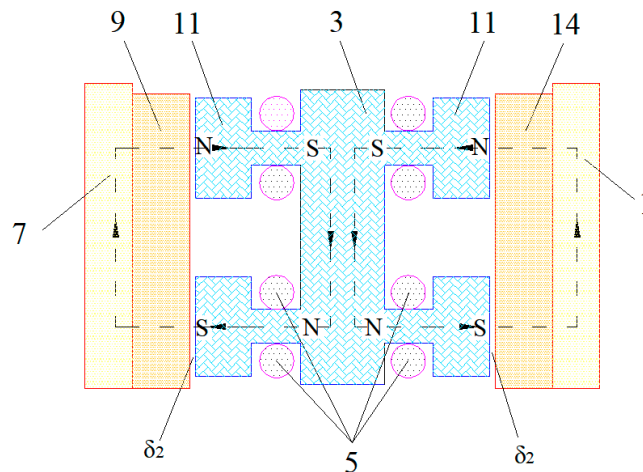


Figure 3. Magnetic circuit diagram of electro-magnetic magnetic field. 1. Outer disk rotor, 3. Combined stator core, 5. Excitation windings, 7. Inner disk rotor, 9. Inner rotor tooth, 11. Excitation core, 14. Outer rotor teeth.

4. Design of Structural Parameters

4.1. Determination of Performance Parameter Index

The generator for the range extender designed in this paper is used in low-speed electric vehicles, widely used by elderly drivers in China. Its maximum speed is only 40 Km/h, the weight of the vehicle is only 300 kg, and the power of the drive motor is from 1.5 Kw to 3 Kw. Combined with the technical indicators of the model YH3000-DJKT range extender, which is manufactured by Langfang Jintai electric vehicle Co., Ltd. in Langfang City of China the main technical indicators of the disk hybrid excitation generator are determined as shown in Table 1.

Table 1. Main technical indicators.

Technical Indicators	Value	Technical Indicators	Value
Rated voltage	72 V	Number of phases	3
Rated power	3000 W	operating mode	continuous duty
Rated speed	3300 r/min	Operating temperature	From −40 °C to 75 °C
Insulation class	E Class	Protection level	IPX4

The rated power of the disk hybrid excitation generator is 3000 W in this paper. To reduce excitation loss, the permanent magnet is used as the main excitation source, and the electrical excitation is used as the auxiliary excitation source. Therefore, the rated power of the permanent magnet is 2000 W, while the rated power of the electrical excitation is 1000 W.

4.2. Parameter Design of Permanent Magnet

The volume of the permanent magnet was calculated via the short-circuit triangle method [22] according to Formula (1):

$$V_M = \frac{(P_N)_{\cos\varphi=0} \sigma_0 C_F K}{3.54 k_B f B_M H_M} \cdot \frac{k_i^2}{k_i - 1} \cdot 10^8 \quad (1)$$

where P_N is the power factor of the generator when $\cos\varphi = 0$, $P_N = 2000$ W; σ_0 is the magnetic leakage coefficient, $\sigma_0 = 1.4$; C_F is the magnetic potential coefficient, $C_F = 1.11$; α is the pole-arc coefficient, $\alpha = 0.8$; K is the magnetic potential conversion coefficient of the direct axis armature reaction, $K = \frac{\alpha\pi + \sin\alpha\pi}{4\sin\frac{\alpha\pi}{2}} = \frac{0.8\pi + \sin 0.64\pi}{4\sin 0.4\pi} = 0.9$; K_B is the waveform factor when the magnetic field waveform is sine, $K_B = 1.11$; f is the frequency, $f = \frac{pn}{60} = 440$; p is the number of pole-pairs, $p = 8$; n is the generator's rated speed; k_i is the short-circuit current multiple, where the value of k_i is taken to be four to obtain a higher voltage adjustment rate; B_M is the magnetic induction intensity of the no-load operating points of the permanent magnet, $B_M = 0.85$ Br and $Br = 1.12 \times 10^4$ Gauss; H_M is the magnetic field intensity in the permanent magnet in the steady short circuit, $H_M = 0.65 H_c$, where $1 \text{ Ost} = 80 \text{ A/m}$ and coercive force $H_c = 9950 \text{ Ost}$; and $\cos\varphi$ is the power factor, $\cos\varphi = 0.85$.

The above data were substituted into Formula (1) to calculate the volume of the permanent magnet: $V_M = 20,834 \text{ mm}^3$.

As $\cos\varphi = 0.85$, according to the relevant literature, when $\cos\varphi > 0$, the influence of the armature reaction on the demagnetization of the permanent magnet weakens, the volume of the permanent magnet is appropriately reduced, and the reduction values are ΔV_M and $\Delta V_M = 0.125 V_M$, so $V_M = 20,834 \times (1 - 0.125) = 1.823 \times 10^4 \text{ mm}^3$.

The structural parameter design of the permanent magnets is usually divided into three parts: the length of magnetization direction, radial cross-sectional area, and axial length. Here, the axial length is equal to the axial length of the combined stator core.

Using the permanent magnet's total volume, the volume of each pair of permanent magnets is calculated, and the calculation method is shown in Formula (2).

$$V_a = \frac{V_m}{p} \quad (2)$$

where V_a is the volume of each antipode of the permanent magnets, V_m is the total volume of permanent magnet, and p is the number of pole-pairs. Using this calculation, the volume of each antipode of the permanent magnets was determined to be 2278 mm^3 .

After calculating the assigned volume of each antipode of the permanent magnets, we determined the structural parameters of each permanent magnet; here, the magnetic potential provided by each pole was first calculated, and then the magnetization direction length and radial cross-sectional area were calculated according to the magnetic potential provided. According to Formula (3), the required magnetic potential of the permanent magnet for a pair of external magnetic paths under a rated load is calculated.

$$F_M = F_\delta K_a K_s = \frac{2}{\mu_0} K_a K_s K_\delta \delta B_\delta \quad (3)$$

where F_δ is the magnetic potential drop under an antipode, $F_\delta = 2K_\delta \delta H_\delta = \frac{2}{\mu_0} K_\delta \delta B_\delta$; H_δ is the magnetic field intensity in the air gap; K_a is the increasing coefficient required to determine the magnetic potential of the permanent magnet to overcome the demagnetization of the armature reaction; K_a is 1.1; K_s is the magnetic circuit saturation coefficient, $K_s = 1.1$; K_δ

is the air gap coefficient, $K_\delta = 1.2$; δ is the length of the air gap, $\delta = 0.5$; B_δ is the magnetic induction intensity in the air gap, $B_\delta = 0.9$ T; and μ_0 is the permeability in the vacuum, $\mu_0 = 4\pi \times 10^{-7}$ H/m.

The magnetic potential required by the permanent magnet for an antipode outer magnetic circuit under the rated load is 1035 A.

The length of magnetization direction, radial cross-sectional area, and magnetic flux of each pole in the air gap of the permanent magnet were calculated using the formulas below. Formula (4) was used to calculate the magnetization length of the permanent magnet, Formula (5) was used to calculate the radial cross-sectional area of the permanent magnet, and Formula (6) was used to calculate the air gap flux per pole.

$$b_M = \frac{F_M}{H_M} \quad (4)$$

$$S_M = \frac{V_a}{b_M} \quad (5)$$

$$\phi_\delta = \frac{B_M S_M}{\sigma_0} \quad (6)$$

where b_M is the magnetization length of permanent magnet, S_M is the radial cross-sectional area of permanent magnet, ϕ_δ is the air gap flux per pole, σ_0 is the magnetic leakage coefficient, and H_M and B_M are the magnetic field intensity and magnetic induction intensity of the permanent magnet at the operating point.

We calculated that the length of magnetization direction of permanent magnet was 2 mm, the radial cross-sectional area of permanent magnet was 1139 mm², and the air-gap flux per pole was 774.5×10^{-6} Wb.

According to design experience and the parameters of the combined stator core, we determined the internal radius of the tile-shaped permanent magnet R_1 to be $R_1 = 120$ mm.

The axial length of the permanent magnet was calculated based on Formula (7), and the outer radius of the tile-shaped permanent magnet was calculated based on Formula (8).

$$R_2 = R_1 + b_M \quad (7)$$

$$L_a = \frac{V_a}{(\pi R_2^2 - \pi R_1^2) \frac{30^\circ}{360^\circ}} \quad (8)$$

where R_2 is the external radius of the tile-shaped permanent magnet, b_M is the length of the magnetization direction of the permanent magnet, R_1 is the internal radius of the tile-shaped permanent magnet, L_a is the axial length of the tile-shaped permanent magnet, V_a is the volume of the permanent magnets per antipode. We calculated that $R_2 = 122$ mm and $L_a = 18$ mm.

4.3. Structural Parameter Design of the Magnetic Yoke

The magnetic yoke is tile-shaped and made of steel material. The inner cambered surface is fitted to the cambered surface of the permanent magnet, and the outer cambered surface is fitted to the inner cylinder surface of the non-magnetic shell. The number of magnetic yokes is eight, the radians of the magnetic yoke and the permanent magnet are 30°, and the position of the magnetic yoke corresponds to that of the permanent magnet, being evenly distributed on the circumference.

According to Formula (9), the axial cross-sectional area S_1 of the magnetic yoke can be calculated as follows:

$$\frac{\phi_\delta}{2} = B_s S_1 \quad (9)$$

where ϕ_δ is the magnetic flux of the permanent magnet per pole in the air gap; B_s is the magnetic induction intensity in the magnetic yoke, $B_s = 0.7$ Br; and S_1 is the axial cross-sectional area of the magnetic yoke.

We calculated the axial cross-sectional area of the magnetic yoke S_1 to be 494 mm^2 , with the inner radius of the yoke being 122 mm .

The outer radius R_5 and thickness h_b of the magnetic yoke are calculated according to Formulas (10) and (11):

$$S_1 = (\pi R_5^2 - \pi R_4^2) \times \frac{30^\circ}{360^\circ} \quad (10)$$

$$R_5 = R_4 + h_b \quad (11)$$

where S_1 is the axial cross-sectional area of the magnetic yoke, R_5 is the outside radius of the magnetic yoke, R_4 is the inner radius of the magnetic yoke, and h_b is the thickness per magnetic yoke.

The outer radius of the yoke R_5 is 129.5 mm , and the thickness of the yoke h_b is 7.5 mm .

According to the overall size of the disk hybrid excitation generator, the axial length of the yoke L_V is 99 mm .

4.4. Parameter Design of Electro-Magnetic Winding

The electro-magnetic winding was wound on the excitation coil bracket, and the adjacent electro-magnetic winding was connected in series and turned in opposite directions, with the number of turns being the same; therefore, the alternating N pole and S pole arrangement of the electro-magnetic winding is formed.

The number of times that electro-magnetic winding had to be performed was calculated via Kirchhoff's second law [23,24]: $\Sigma HL = \Sigma NI$, $\Sigma \frac{Bl}{u_r u_0} = IN$. Using this equation, we determined that the algebraic sum of magnetic pressure was equal to the algebraic sum of each magnetic flux potential value in a closed magnetic circuit. The following equation describes the electromagnetic characteristics of the magnetic circuit and combines electricity and magnetism:

$$\frac{B_0 l_0}{u_0} + \frac{B_1 l_1}{u_{r1} \cdot u_0} + \frac{B_2 l_2}{u_{r2} \cdot u_0} = IN \quad (12)$$

where B_0 is the magnetic induction intensity in the air gap; B_1 is the magnetic induction intensity in the stator; B_2 is the magnetic induction intensity in the rotor, $B_0 = B_1 = B_2 = 0.85 \text{ T}$; l_0 is the length of the air gap magnetic circuit, $l_0 = 2\delta = 1 \text{ mm}$; l_1 is the length of the magnetic circuit in the stator, $l_1 = 200 \text{ mm}$; l_2 is the length of the magnetic circuit in the rotor, $l_2 = 160 \text{ mm}$; μ_0 is the permeability in the vacuum, $\mu_0 = 4\pi \times 10^{-7} \text{ H/m}$; u_{r1} is the relative permeability of the stator, $u_{r1} = \frac{u_{Fe1}}{\mu_0} = 200$; u_{r2} is the relative permeability of the rotor, $u_{r2} = \frac{u_{Fe2}}{\mu_0} = 8000$; I is the current in the electro-magnetic winding, $I = 1.5 \text{ A}$; and N is the number of times that electro-magnetic winding was performed.

We calculated that number of turns of electro-magnetic winding N was performed 566 times. Thus, number of turns per pole of electro-magnetic winding is 75.

4.5. Design of Wire Embedding Mode of Armature Winding

The armature winding includes single-layer winding, double-layer winding, and mixed winding. Depending on the winding shape and embedding method of the coil, it can be subdivided into two types: fractional slot concentrated winding and distributed winding [25,26]. Single- or double-layer winding is generally used in the generator; the single-layer winding method is simple and the utilization rate of slots is high, though the coil cannot easily achieve mutual inductance, whereas double-layer winding produces good electromotive force with a sine waveform and its pitch is easy to adjust. The disk hybrid excitation generator presented in this paper uses the single-layer fractional slot concentrated winding method and star connection mode, and its winding pitch is one.

The advantages of fractional slot concentrated winding are as follows: each winding only occurs around one magnetic tooth, the end of the winding is short, and copper consumption is reduced; the coil is simple to manufacture and maintain; the tooth is wide and not easy to saturate; and the utilization rate of slots is high. An illustration of armature winding is shown in Figure 4.

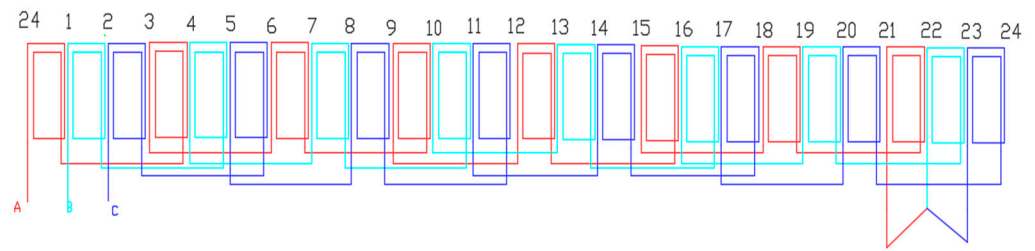


Figure 4. The unfolded drawing of armature winding.

5. Finite Element Analysis of Magnetic Field

The disk hybrid excitation generator has a complex structure, while that of the magnetic field distribution is three-dimensional. Moreover, a magnetic saturation phenomenon occurs, and it is nonlinear, meaning that it cannot be obtained via an analytical method. Finally, the finite element method is a variation-based numerical calculation method, and the electromagnetic field’s accurate distribution is obtained via such a method.

5.1. Finite Element Equation of Three-Dimensional Magnetic Field

The rotor structure of the disk hybrid excitation generator used in an EREV range extender is complicated, meaning that the distribution of the magnetic field is also complicated, as it presents obvious three-dimensional field characteristics and is difficult to analyze and calculate. As the vector A in the three-dimensional field includes the components x , y , and z , the application of the finite element method is more complicated than for the two-dimensional field [27,28].

When the static field is analyzed, the magnetic field in the motor becomes a three-dimensional constant magnetic field or a radial stretching of a two-dimensional magnetic field, and the magnetic field intensity H and current density J satisfy the Ampere loop law.

$$\nabla \cdot H = J \tag{13}$$

According to the law of magnetic flux continuity

$$\nabla \cdot B = 0 \tag{14}$$

where B is the magnetic induction intensity, for $H = B/\mu$, μ is the magnetic conductivity, and for $B = \Delta \times A$, A is the vector potential. By substituting $H = B/\mu$ and $B = \Delta \times A$ into Formula (13), Formula (15) can be obtained as follows:

$$\nabla \cdot \left(\frac{1}{\mu} \nabla \times A \right) = J \tag{15}$$

If the magnetic resistance is $v = 1/\mu$, by substituting $v = 1/\mu$ into Formula (15), Formula (15) can be expressed as follows:

$$\nabla \cdot (v \nabla \times A) = J \tag{16}$$

$$A = \begin{bmatrix} A_x \\ A_y \\ A_z \end{bmatrix}, J = \begin{bmatrix} J_x \\ J_y \\ J_z \end{bmatrix}, v = \begin{bmatrix} v_x & 0 & 0 \\ 0 & v_y & 0 \\ 0 & 0 & v_z \end{bmatrix} \tag{17}$$

After substituting A, J , and v in Formula (17) into Formula (16), Formula (16) is expanded, and three partial differential equations are obtained, which are Formulas (18)–(20).

$$\frac{\partial}{\partial y} \left[v_z \left(\frac{\partial A_y}{\partial x} - \frac{\partial A_x}{\partial y} \right) \right] - \frac{\partial}{\partial z} \left[v_y \left(\frac{\partial A_x}{\partial z} - \frac{\partial A_z}{\partial x} \right) \right] = J_x \tag{18}$$

$$\frac{\partial}{\partial z} \left[v_x \left(\frac{\partial A_z}{\partial y} - \frac{\partial A_y}{\partial z} \right) \right] - \frac{\partial}{\partial x} \left[v_z \left(\frac{\partial A_y}{\partial x} - \frac{\partial A_x}{\partial y} \right) \right] = J_y \quad (19)$$

$$\frac{\partial}{\partial x} \left[v_y \left(\frac{\partial A_x}{\partial z} - \frac{\partial A_z}{\partial x} \right) \right] - \frac{\partial}{\partial y} \left[v_x \left(\frac{\partial A_z}{\partial y} - \frac{\partial A_y}{\partial z} \right) \right] = J_z \quad (20)$$

As $B = \Delta \times A$, the components of B in the x , y , and z directions are shown in Formulas (21)–(23).

$$B_x = \frac{\partial A_z}{\partial y} - \frac{\partial A_y}{\partial z} = A_{zy} - A_{yz} \quad (21)$$

$$B_y = \frac{\partial A_x}{\partial z} - \frac{\partial A_z}{\partial x} = A_{xz} - A_{zx} \quad (22)$$

$$B_z = \frac{\partial A_y}{\partial x} - \frac{\partial A_x}{\partial y} = A_{yx} - A_{xy} \quad (23)$$

The magnitude of magnetic induction intensity B is defined as follows:

$$B = \sqrt{(B_x^2 + B_y^2 + B_z^2)} \quad (24)$$

As $H = B/\mu$ and $1/\mu = v$, the expressions of the component of magnetic field intensity H in the x , y , and z directions can be obtained. They are shown in Formulas (25)–(27).

$$H_x = v_x B_x = v_x (A_{zy} - A_{yz}) \quad (25)$$

$$H_y = v_y B_y = v_y (A_{xz} - A_{zx}) \quad (26)$$

$$H_z = v_z B_z = v_z (A_{yx} - A_{xy}) \quad (27)$$

5.2. Establishment of the Finite Element Model

As the structure of the disk hybrid excitation generator is complex, it is difficult to model it using the finite element software; thus, a geometric model of the generator was built using 3D modeling software and imported into the finite element software. Then, the electro-magnetic winding and permanent magnet models were established using the finite element software, and the material properties and magnetization direction were defined. The permanent magnet was made of NdFe35, and the N and S poles were arranged. The direction of magnetization was radial. The combined stator, inner disk rotor, and outer disk rotor component used a silicon steel sheet DW360_51, the magnetic yoke and excitation core are used steel, and the winding used copper. To cut the simulation time, the quarter model of the generator was analyzed. A three-dimension finite element model of the generator is shown in Figure 5.

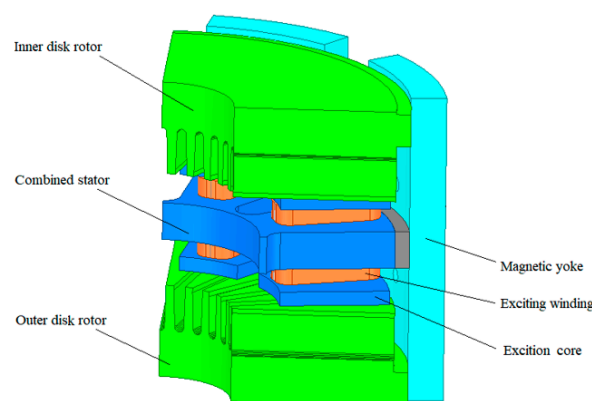


Figure 5. Three-dimensional finite element model of disk hybrid excitation generator.

The finite element grid of the disk hybrid excitation generator is shown in Figure 6. As the rotor of the generator was made of silicon steel, its magnetoresistance was much smaller than that of the air gap, meaning that most of the magnetic field was stored in the air gap [29,30]. For the calculation accuracy, the more grids present in the air gap magnetic field, the higher the calculation accuracy of the model, though the calculation time was also longer. Therefore, considering the accuracy and calculation efficiency, the number of grids in the finite element model was 260,551.

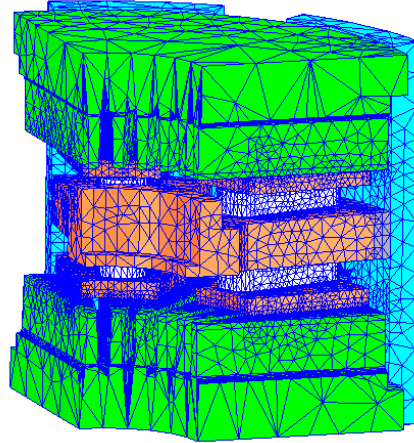


Figure 6. Finite element meshing.

5.3. Magnetic Field Analysis

When the excitation coil was not energized, only the permanent magnetic field generated by the permanent magnet was present in the magnetic circuit. The related magnetic dense cloud is shown in Figure 7. Based on the magnetic dense cloud, the specific distribution of the magnetic field and saturation of each part of the magnetic field could be determined. Based on the magnetic density vector map, the magnitude and direction of the magnetic flux passing through a given area could be obtained. Figure 7 shows that the magnetic field was concentrated and saturated in the part of the combined stator core closed to the central axis (the part marked by a yellow circle). Therefore, that part was optimized, and the radial thickness was increased; the optimized magnetic dense cloud map is shown in Figure 8. At this point, the magnetic saturation phenomenon disappeared. When only the permanent magnet underwent excitation, the effective magnetic field was located in the rotor teeth of the disk rotor; the magnetic density of the disk rotor is shown in Figure 9. At this point, the magnetic field distribution of the disk rotor was more uniform, and the magnetic induction intensity at the edge of the disk rotor near the magnetic yoke was greater, consistent with the actual situation.

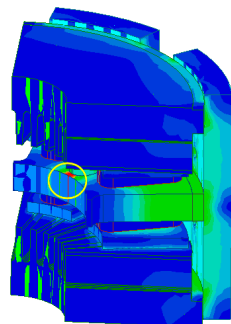


Figure 7. Primitive magnetic dense cloud map.

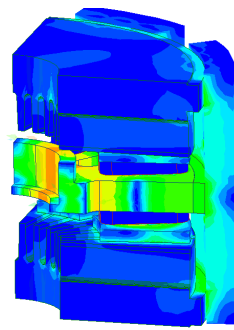


Figure 8. Magnetic dense cloud map optimized.

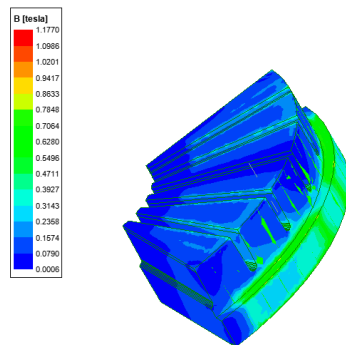


Figure 9. Magnetic density of the disk rotor.

When the current passes into the excitation coil, the increasing effect of the magnetic induction intensity can be achieved, and when the value of the current is different, the effect is different. When 1 A and 2 A is passed through the excitation coil, respectively, magnetic density vector maps and magnetic dense cloud maps on the surface of quarter model are obtained at different currents. They are shown in Figures 10 and 11.

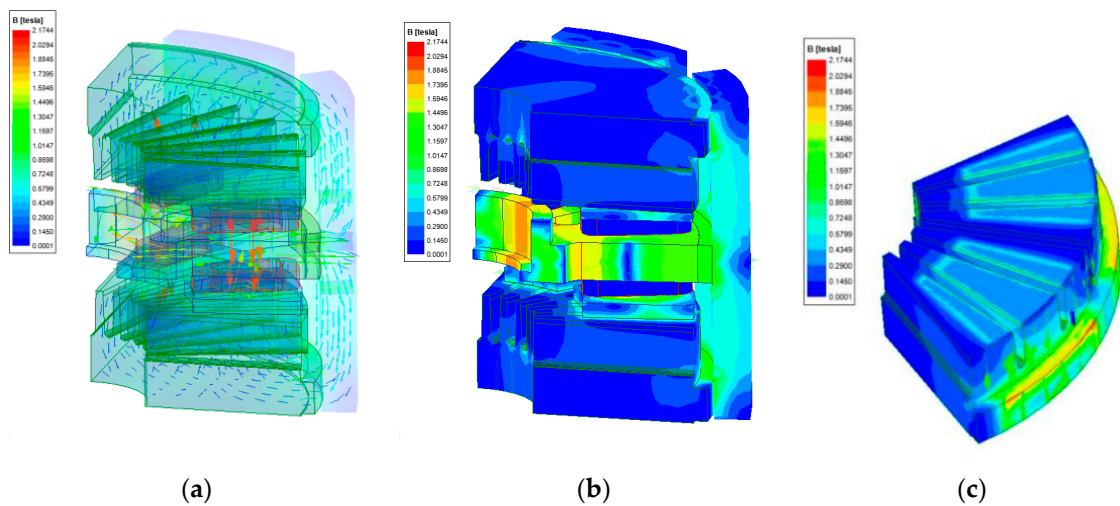


Figure 10. Magnetic density vector map and magnetic dense cloud map when the value of excitation current is 1 A: (a) magnetic density vector; (b) magnetic dense cloud map, (c) magnetic dense cloud map of disk rotor.

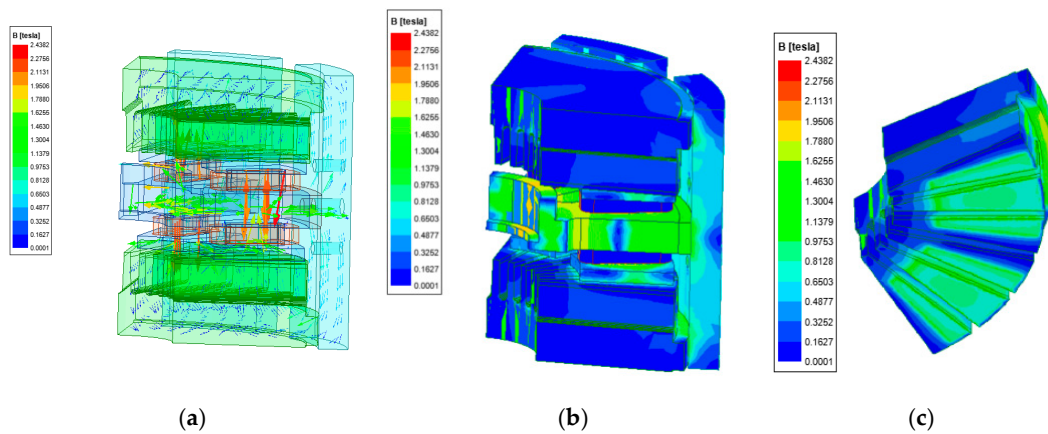


Figure 11. Magnetic density vector map and magnetic dense cloud map when the value of excitation current is 2 A: (a) magnetic density vector; (b) magnetic dense cloud map; (c) magnetic dense cloud map of disk rotor.

The specific values of magnetic induction intensity are shown in Table 2. Figures 8 and 11 show that when the value of excitation current is 0 A, only magnetic flux is generated by the permanent magnet in the model, and the magnetic induction intensity at the stator tooth is 0.7848 T. When the forward current (1 A) passes through the excitation winding, the maximum magnetic induction intensity is 2.1744 T, and the magnetic induction intensity at the stator tooth is 1.1015 T. When the forward current (2 A) passes through the excitation winding, the maximum magnetic induction intensity is 2.4382 T, and the magnetic induction intensity at the stator tooth is 1.4630 T. We can see that the synthetic magnetic induction intensity in the stator tooth increases in line with the increase in the current. Therefore, the effective magnetic flux in the rotor tooth can be adjusted by adjusting the value of the excitation current.

Table 2. Magnetic induction intensity.

Exciting Current (A)	Magnetic Induction Intensity at Stator Tooth (T)	Maximum Magnetic Induction Intensity (T)
0.0	0.7848	1.1770
1.0	1.1015	2.1744
2.0	1.4630	2.4382

6. Equivalent Magnetic Circuit Analysis

6.1. Magnetic Circuit Analysis of the Permanent Magnet Part

The no-load effective magnetic flux was obtained using the working diagram of the magnet. In the process of solving, firstly, the direct axis equivalent magnetic circuit diagram was drawn based on the specific magnetic circuit structure, and then the synthetic permeance G_0 , leakage permeance G_S , and no-load leakage magnetic coefficient σ_0 were calculated [31,32].

For the disk hybrid excitation generator, taking into account the additional air gap between the magnetic yoke and the combined stator core, the additional air gap between the combined stator core and the disk rotor, and the magnetic potential drop of the magnetic yoke and disk rotor, the leakage flux was divided into two categories: ϕ_{S-ys} (between the magnetic yoke and the combined stator core) and ϕ_{S-M} (magnet itself). The corresponding equivalent magnetic circuit diagram for the no-load operation is shown in Figure 12. In Figure 12, the permeance of the magnetic yoke (each) is G_y , the leakage permeance of the permanent magnet is G_{SM} , the leakage permeance between the magnetic yoke and the combined stator core is G_{S-ys} , the permeance between the magnetic yoke and the inner disk rotor is $G_{\delta 1}$, the permeance of the inner disk rotor is G_d , the permeance between the

inner disk rotor and the combined stator core is $G_{\delta 2}$, and the permeance of the combined stator core is G_s .

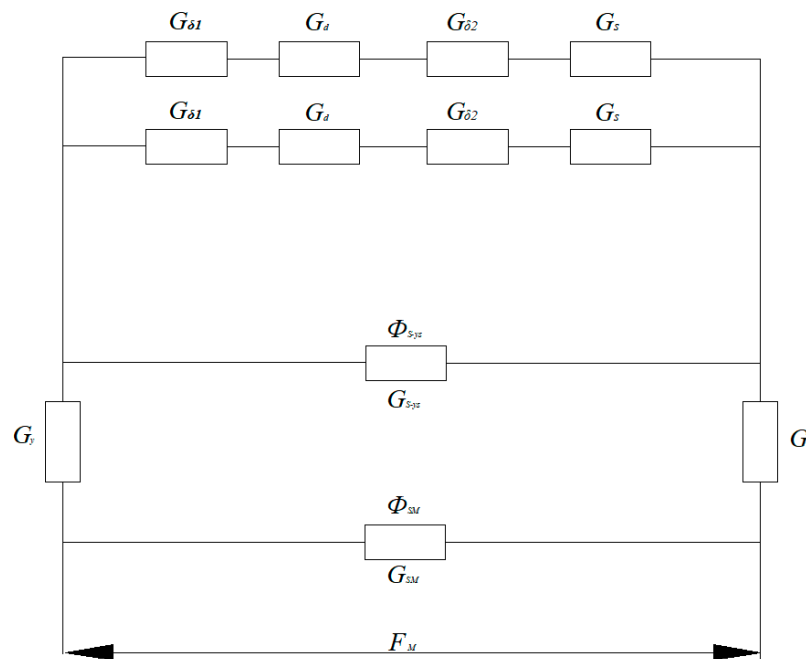


Figure 12. Equivalent magnetic circuit of the permanent magnet part.

By solving Figure 12, the synthetic permeance G_0 was obtained as follows.

$$G_0 = G_{SM} + \frac{1}{\frac{2}{G_y} + \frac{1}{G_{S-ys}} + \frac{1}{\frac{1}{G_{\delta 1}} + \frac{1}{G_d} + \frac{1}{G_{\delta 2}} + \frac{1}{G_s}} + \frac{1}{\frac{1}{G_{\delta 1}} + \frac{1}{G_d} + \frac{1}{G_{\delta 2}} + \frac{1}{G_s}}} \quad (28)$$

The leakage permeance G_s was obtained as follows.

$$G_s = G_{SM} + G_{S-ys} \times \left[\frac{\frac{1}{2} \left(\frac{1}{G_{\delta 1}} + \frac{1}{G_d} + \frac{1}{G_{\delta 2}} + \frac{1}{G_s} \right)}{\left(\frac{2}{G_y} + \frac{1}{2} \left(\frac{1}{G_{\delta 1}} + \frac{1}{G_d} + \frac{1}{G_{\delta 2}} + \frac{1}{G_s} \right) \right) + G_{S-ys} \left(\frac{2}{G_y} \right) \frac{1}{2} \left(\frac{1}{G_{\delta 1}} + \frac{1}{G_d} + \frac{1}{G_{\delta 2}} + \frac{1}{G_s} \right)} \right] \quad (29)$$

The no-load magnetic leakage coefficient σ_0 was obtained as follows.

$$\sigma_0 = 1 + (G_{SM} + G_{S-ys}) \left(\frac{2}{G_{\delta 1}} + \frac{2}{G_d} + \frac{2}{G_{\delta 2}} + \frac{2}{G_s} \right) + G_{SM} \frac{2}{G_y} \left[1 + G_{S-ys} \left(\frac{2}{G_{\delta 1}} + \frac{2}{G_d} + \frac{2}{G_{\delta 2}} + \frac{2}{G_s} \right) \right] \quad (30)$$

Based on Kirchhoff's first law and Ohm's magnetic circuit law, the following simultaneous equations could be used:

$$\begin{cases} F_{M0} = (\phi_M - \phi_{sM}) \left(\frac{2}{G_y} \right) + \frac{1}{2} \cdot \phi_U \left(\frac{1}{G_{\delta 1}} + \frac{1}{G_d} + \frac{1}{G_{\delta 2}} + \frac{1}{G_s} \right) \\ F_{M0} = \frac{\phi_{sM}}{G_{sM}} \end{cases} \quad (31)$$

We determined via Formula (30) that:

$$(\phi_M - \phi_{sM}) \left(\frac{2}{G_y} \right) + \frac{\phi_{s-ys}}{G_{s-ys}} - \frac{\phi_{sM}}{G_{sM}} = 0 \quad (32)$$

Due to $\phi_M = \phi_U + \phi_{s-ys} + \phi_{sM}$. Through an algebraic operation, the solutions to the simultaneous equations were solved. As $\phi_M = F_M G$

$$\phi_{s0} = \phi_{s-ys} + \phi_{sM} = F_M G_s \quad (33)$$

$$\phi_{U0} = \phi_M - \phi_s = F_M(G - G_s) = F_M G_U \tag{34}$$

where G is the synthetic permeance, G_s is the synthetic leakage permeance, and G_U is the effective permeance. Here, F_M , G , and G_s were substituted into Formula (31), and the total flux, leakage flux, and effective flux of the permanent magnet part were obtained.

6.2. Magnetic Circuit Analysis of the Electro-Magnetic Part

The equivalent magnetic circuit diagram of the electro-magnetic part is shown in Figure 13. In Figure 13, the permeance of the magnetic yoke (each) is G_y , the leakage permeance of the permanent magnet is G_{SE} , the leakage permeance between the disk rotor and the combined stator core is G_{s-ds} , the permeance between the disk rotor and the inside disk rotor is $G_{\delta 1}$, the permeance of the disk rotor is G_d , the permeance between the disk rotor and the combined stator core is $G_{\delta 2}$, the permeance of the combined stator core is G_s , and the permeance of the permanent magnet is G_M . The synthetic magnetic permeance G_0 , synthetic magnetic leakage permeance G_s , and no-load magnetic leakage coefficient σ_0 of electro-magnetic part were obtained by analyzing Figure 13.

$$G_0 = G_{SE} + \frac{1}{\frac{1}{G_{\delta 2}} + \frac{1}{G_{s-ds} + \frac{1}{\frac{1}{\frac{1}{G_{\delta 1}} + \frac{1}{G_d} + \frac{1}{G_y} + \frac{1}{G_M} + \frac{1}{G_s}}}}} \tag{35}$$

$$G_s = G_{SE} + G_{s-ds} \times \left[\frac{1}{1 + \frac{\frac{1}{G_{\delta 2}}}{\frac{1}{G_{\delta 1}} + \frac{1}{G_d} + \frac{1}{G_y} + \frac{1}{G_M} + \frac{1}{G_s}} + G_{s-ds} \frac{1}{G_{\delta 2}}} \right] \tag{36}$$

$$\sigma_0 = 1 + (G_{SE} + G_{s-ds}) \left(\frac{1}{G_{\delta 1}} + \frac{1}{G_d} + \frac{1}{G_y} + \frac{1}{G_M} + \frac{1}{G_s} \right) + G_{SE} \left(\frac{1}{G_{\delta 2}} \right) \left[1 + G_{s-ds} \left(\frac{1}{G_{\delta 1}} + \frac{1}{G_d} + \frac{1}{G_y} + \frac{1}{G_M} + \frac{1}{G_s} \right) \right] \tag{37}$$

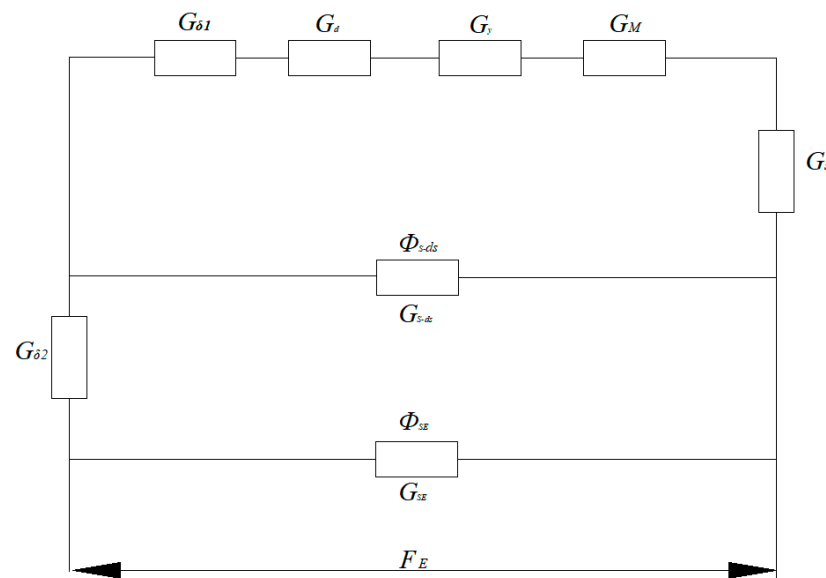


Figure 13. Equivalent magnetic circuit of electro-magnetic part.

7. Comparative Analysis of the Calculation Results of the Two Methods

The air gap flux and flux density in no-load conditions and the flux density of the rotor teeth and rotor yoke of the generator were obtained using the field calculator of the finite element software [33,34]. The magnetic density in the finite element software was compared with the magnetic density in the equivalent magnetic circuit analysis. The flux

densities of each part under no-load conditions are shown in Figure 14. In Figure 14, EMCM stands for the equivalent magnetic circuit method, while FEM stands for the finite element method. We can see that the calculated results of the equivalent magnetic circuit are similar to those of the finite element simulation, and the synthetic magnetic fields of each part calculated via equivalent magnetic circuit methods are slightly higher than those calculated via the finite element method. The synthetic magnetic field in the air gap increased with the increase in the excitation current. Thus, the output voltage and power also increased. Therefore, the method of field-circuit combining for designing the generator was reasonable and effective, and the increase in the excitation current improved the output power and voltage of the generator.

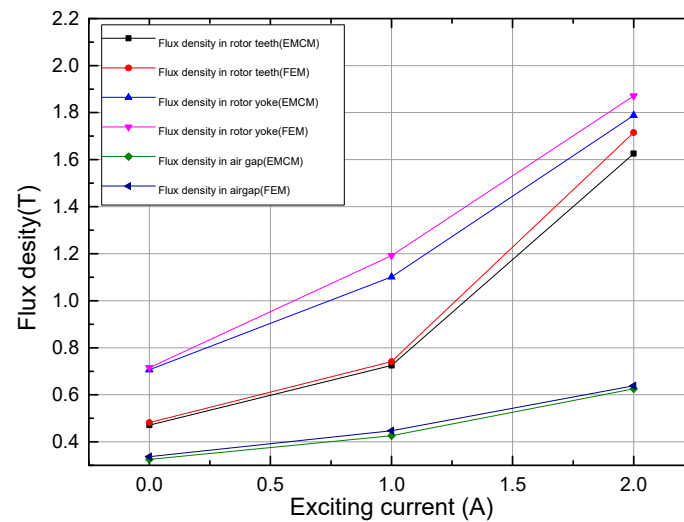


Figure 14. The magnetic density of each part on no-load.

8. Conclusions

To overcome the defects of the generator used in a EREV range extender, a new type of disk hybrid excitation generator was proposed; the axial dimension of the generator was reduced and the radial space of the range extender bin was used effectively in the structure, making it especially suitable for use in an EREV range extender.

- (1) Though the magnetic circuit of the disk hybrid excitation generator was analyzed, we found that the electro-magnetic flux did not pass through the permanent magnet, preventing the electro-magnetic field from influencing the permanent magnet and reducing the occurrence of irreversible demagnetization, although the axial magnetic flux and radial magnetic flux of the disk hybrid excitation generator share part of the magnetic circuit. Combined with magnetic circuit analysis, the operating principle of the disk hybrid excitation generator was also analyzed.
- (2) According to the requirements of the existing EREV power supply system, the performance indicators of the disk hybrid excitation generator and the power distributions of the electro-magnetic part and permanent magnet part were determined, and the structural parameters of the disk hybrid excitation generator were set. The generator's three-dimensional geometric model was established based on the results.
- (3) To further optimize the structure of the generator, the equivalent magnetic circuit models of the permanent magnet and the electro-magnetic parts of the disk hybrid excitation generator were established, and the equivalent magnetic circuit model was analyzed via Kirchhoff's first law and Ohm's magnetic circuit law. The formulas for total flux, leakage flux, and effective flux were derived.
- (4) According to the structural characteristics of the disk hybrid excitation generator, a three-dimensional finite element model was established, and the structural parameters were optimized through finite element analysis, eliminating the magnetic circuit's

saturation. The synthetic magnetic field under different currents was analyzed, and we confirmed that the synthetic magnetic field could be effectively adjusted by adjusting the excitation current. We also confirmed that the operating principle of the generator was reasonable.

- (5) The equivalent magnetic circuit and finite element methods were used to calculate the magnetic density of the air gap δ_2 , the rotor tooth, and the rotor yoke under no-load conditions, and a comparative analysis was performed. The results of the equivalent magnetic circuit method mirror the results of the finite element simulation, proving that the established equivalent magnetic circuit and finite element models were relatively accurate.

The design and magnetic circuit analysis methods for the disk hybrid excitation generator are provided, providing theoretical support for the design and development of a disk hybrid excitation generator for use in a range extender in an EREV. The generator's application will boost the range extender's performance in extended-range electric vehicles.

Funding: Science and Technology Research Project of Colleges and Universities of Hebei Province, grant number QN2019205; Xingtai Youth Talent Plan Project, grant number 2021ZZ034.

Data Availability Statement: The data presented in this study are available on request from the corresponding author due to privacy.

Conflicts of Interest: The author declares no conflicts of interest.

References

1. De Wolf, D.; Smeers, Y. Comparison of Battery Electric Vehicles and Fuel Cell Vehicles. *World Electr. Veh. J.* **2023**, *14*, 262. [[CrossRef](#)]
2. Jia, L. Optimization Effect of the Improved Power System Integrating Composite Motors on the Energy Consumption of Electric Vehicles. *World Electr. Veh. J.* **2023**, *14*, 257. [[CrossRef](#)]
3. Li, Y.J.; Li, W.M.; Zhu, Y.D. Parameter matching and simulation of power system of extended-range electric vehicle. *Mod. Mach.* **2023**, *04*, 16–20.
4. Zhang, W.J.; He, Y.T. Standards and Industry Status of Range-extended Electric Vehicle. *Auto* **2023**, *3*, 3–6.
5. Xia, C.; Bi, J.; Shi, J. Investigation of a Cup-Rotor Permanent-Magnet Doubly Fed Machine for Extended-Range Electric Vehicles. *Energies* **2023**, *16*, 2455. [[CrossRef](#)]
6. Lin, W.; Zhao, H.; Zhang, B.; Wang, Y.; Xiao, Y.; Xu, K.; Zhao, R. Predictive Energy Management Strategy for Range-Extended Electric Vehicles Based on ITS Information and Start-Stop Optimization with Vehicle Velocity Forecast. *Energies* **2022**, *15*, 7774. [[CrossRef](#)]
7. Hu, W.J.; Zhang, X.Y.; Geng, H.H.; Gao, T.; Shi, L.W.; You, D. Electromagnetic Design and Flux Regulation Analysis of New Hybrid Excitation Generator for Electric Vehicle Range Extender. *J. Electr. Comput. Eng.* **2021**, *2021*, 5547517. [[CrossRef](#)]
8. Shangguan, X.F.; Wang, Y.C. Optimization of axial flux permanent magnet synchronous generator. *Electron. Meas. Technol.* **2017**, *9*, 52–59.
9. Asefi, T.; Faiz, J.; Khan, M. Design of Dual Rotor Axial Flux Permanent Magnet Generators with Ferrite and Rare-Earth Magnets. In Proceedings of the 2018 IEEE 18th International Power Electronics and Motion Control Conference (PEMC), Budapest, Hungary, 26–30 August 2018; IEEE: Piscataway, NJ, USA, 2018; pp. 531–538.
10. Hou, Y.; Yao, D.W.; Wu, F.; Lv, C.L.; Wang, H.; Shen, J.H. Control strategy for electric vehicle range extender based on hybrid excitation generator. *J. Shanghai Jiaotong Univ.* **2021**, *55*, 206–212.
11. Wu, W.Q.; Zhu, X.Y.; Xiang, Z.X.; Quan, L. Design and Analysis of a Less-Rare-Earth Permanent Magnet Brushless Motor with Hybrid Permanent Magnets. *Electr. Mach. Control Appl.* **2018**, *45*, 73–78.
12. Ishii, S.; Yu, H.; Nakamura, K. Characteristics of novel flux barrier type outer rotor IPM motor with rare-earth and ferrite magnets. In Proceedings of the International Conference on Renewable Energy Research & Applications, Madrid, Spain, 20–23 October 2013.
13. Chu, Q.; Che, S.; Li, C.Y. Optimization design of less-rare-earth Halbach permanent magnet synchronous motor with module poles. *Electr. Mach. Control Appl.* **2023**, *50*, 22–28.
14. Wu, Z.Z.; Zhu, Z.Q. Design and Analysis of a Novel Partitioned Stator Hybrid Excitation Machine. *Proc. CSEE* **2017**, *37*, 6543–6556.
15. Lee, J.H.; Yun, T.W.; Jeon, A.R. Characteristic analysis & optimum design solutions of Permanent Magnet Assisted Synchronous Reluctance Motor for power improvement. In Proceedings of the 2010 International Conference on Electrical Machines and Systems, Incheon, Republic of Korea, 10–13 October 2010; Electromagnetic Field Computation.
16. Zhu, X.; Yang, S.; Du, Y.; Xiang, Z.X.; Xu, L. Electromagnetic Performance Analysis and Verification of a New Flux-Intensifying Permanent Magnet Brushless Motor with Two-Layer Segmented Permanent Magnets. *IEEE Trans. Magn.* **2016**, *52*, 1–4. [[CrossRef](#)]
17. Guglielmi, P.; Boazzo, B.; Armando, E. Permanent-Magnet Minimization in PM-Assisted Synchronous Reluctance Motors for Wide Speed Range. *IEEE Trans. Ind. Appl.* **2013**, *49*, 31–41. [[CrossRef](#)]

18. Zhao, J.L.; Quan, X.W.; Lin, M.Y. Design and Analysis of a Double-rotor Hybrid Excited Axial Switched-flux Permanent Magnet Machine. *Proc. CSEE* **2020**, *40*, 7860–7868+8223.
19. Chen, Y.Y.; Cai, T.L.; Li, M.Y. Analysis of a Less-rare-Earth Hybrid Magnet Motor Based on Coupling Simulation. *Mach. Tool Hydraul.* **2022**, *50*, 120–124.
20. Levin, N.; Orlova, S.; Pugachov, V.; Ribickis, L. Optimization of the magnetic circuit of the homopolar inductor machine with non-overlapping concentrated windings. In Proceedings of the 14th International Power Electronics and Motion Control Conference, Ohrid, Macedonia, 6–8 September 2010.
21. Dmitrievskii, V.; Prakht, V.; Anuchin, A.; Kazakbaev, V. Design Optimization of a Traction Synchronous Homopolar Motor. *Mathematics* **2021**, *9*, 1352. [[CrossRef](#)]
22. Tang, R.Y. *Theory and Design of Modern Permanent Magnet Motor*, 2nd ed.; China Machine Press: Beijing, China, 2019.
23. Wang, X.H. *Permanent Magnet Motor*; China Electric Power Press: Beijing, China, 2023.
24. Stephen, D.U. *Electric Machinery*; Publishing House of Electronics Industry: Beijing, China, 2021.
25. Decner, A.; Baranski, M.; Jarek, T.; Berhausen, S. Methods of Diagnosing the Insulation of Electric Machines Windings. *Energies* **2022**, *15*, 8465. [[CrossRef](#)]
26. Selema, A.; Ibrahim, M.N.; Sergeant, P. Electrical Machines Winding Technology: Latest Advancements for Transportation Electrification. *Machines* **2022**, *10*, 563. [[CrossRef](#)]
27. Jiang, J.C.; Shi, Z.C.; Lin, X.G.; Zheng, Q.G.; Xie, W. Application Design and Analysis of FSCW PMSM Based on Stator Flux Barrier. *Electr. Mach. Control Appl.* **2021**, *48*, 68–72+83.
28. Mirosław, G.; Marek, P.M.; Andrzej, D. The Modeling of Magnetic Fields in Electromagnetic Microgenerators Using the Finite Element Method. *Energies* **2022**, *15*, 1014.
29. Tong, W.M.; Jing, M.A. Quasi-3-D analytical model of magnetic field for axial-flux motor based on conformal mapping method considering end effect. *Electr. Mach. Control* **2021**, *25*, 47–55.
30. Ku, J.; Lei, Z.; Lin, H.; Yan, Q.X.; Chen, H.H.; Guo, B. Interaction of magnetic spheres in magnetic fields from the view of magnetic energy density: A 3D finite element analysis (FEA). *Int. J. Min. Sci. Technol.* **2022**, *32*, 1341–1350. [[CrossRef](#)]
31. Dou, Y.; Li, Y.J.; Yue, S.C.; Li, Y.; Zhu, J.G. Measurement of alternating and rotational magnetostrictions of non-oriented silicon steel sheets. *J. Magn. Magn. Mater.* **2023**, *571*, 170566. [[CrossRef](#)]
32. Liu, C.C.; Chao, Z.; Wang, S.P.; Wang, Y.H. A quick electromagnetic performance analysis method for permanent magnet claw pole machine based on combined analytical and equivalent magnetic circuit method. *Electr. Eng.* **2023**, *105*, 1541–1553. [[CrossRef](#)]
33. Jiang, J.G.; Zeng, Z.F.; Fu, Y.H.; Zhang, E.L.; Long, D.H. MCR-WPT System Simulation Based on ANSYS Electronics Desktop/Maxwe113D. *Control Instrum. Chem. Ind.* **2021**, *48*, 634–639.
34. Meng, F.Y.; Pu, Z.M.; Ma, C. Ansoft Maxwell-based Finite Element Analysis of a Permanent Magnet DC Hollow Cup Motor. *Micromotors* **2023**, *56*, 8–11.

Disclaimer/Publisher’s Note: The statements, opinions and data contained in all publications are solely those of the individual author(s) and contributor(s) and not of MDPI and/or the editor(s). MDPI and/or the editor(s) disclaim responsibility for any injury to people or property resulting from any ideas, methods, instructions or products referred to in the content.